Research Square

Preprints are preliminary reports that have not undergone peer review.
They should not be considered conclusive, used to inform clinical practice,
or referenced by the media as validated information.

Experimental and Modelling Analysis of Electrolyte Effects in Zinc-Modified MnO_2/Graphene Symmetric Supercapacitor

K. N. Unnimaya
University College
Elsa Dais
Indian Institute of Space Science and Technology
Riswana N L N L
University College
Sandhya Karunakaran Yesodha
Indian Institute of Space Science and Technology
V. Vipin Das
University College
C. S Preenu
University College
Gopinathan Anoop
Amrita Vishwa Vidyapeetham
Janardhanan R Rani
ranijnair@gmail.com
University College

Research Article

Keywords: symmetric supercapacitor, Zn-doped MnO2, graphene, KOH, Na_2SO_4, BJH pore-size distribution, aqueous electrolyte, electrochemical impedance

Posted Date: November 11th, 2026

DOI: https://doi.org/10.21203/rs.3.rs-11469030/v1

License: This work is licensed under a Creative Commons Attribution 4.0 International License.
Read Full License

Additional Declarations: No competing interests reported.

Abstract

Aqueous symmetric supercapacitors are promising and sustainable energy storage devices with low cost, low toxicity, operational safety and simple design, using the same active material in both electrodes. Here, we investigate the effect of electrolyte on the interfacial charge storage by testing zinc-doped manganese dioxide/graphene (Zn-MnO_2/G) nanocomposite electrodes in symmetric cells using KOH and Na_2SO_4 electrolyte. The composite combined the pseudocapacitive redox activity of MnO_2 with the electronic conductivity and surface accessibility of graphene, and the Zn incorporation was intended to modify the local defect chemistry and charge-transfer behavior. Nitrogen adsorption-desorption analysis suggested mesoporous texture with cumulative pore volume of 0.0453 $cm^3\ g^{-1}$, pore surface area of about 13.0 $m^2\ g^{-1}$ and dominant pore width of about 3.38 nm that can facilitate electrolyte penetration and access to redox-active sites. Electrochemical measurements demonstrated that the studied symmetric cell configuration showed electrolyte-dependent capacitive behavior. The KOH-based device showed lower impedance, more favorable capacitive relaxation and better energy-density retention than the Na_2SO_4based device. The rate-capability fitting also showed a smaller rate-induced energy loss in KOH. The improvement in the porous Zn-MnO_2/G electrode was ascribed to more favorable ion transport, lower interfacial resistance and more efficient utilization of Mn redox-active sites in the alkaline electrolyte. These results suggest that the device-level performance of Zn-MnO_2/G symmetric supercapacitors is significantly affected by the electrolyte selection.

1.Introduction

Electrochemical (EC) supercapacitors (SCs) are increasingly important complementary energy-storage devices for applications requiring rapid charging, high power delivery, and long operational life. Their performance lies between that of conventional dielectric capacitors and rechargeable batteries: they store more energy than ordinary capacitors while generally providing faster charge–discharge kinetics and better cycling stability than batteries [1–6]. Charge storage occurs through electric double-layer capacitance at the electrode–electrolyte interface, fast surface or near-surface faradaic reactions, or a combination of both mechanisms [5–11].

Aqueous electrolytes are particularly attractive because of their high ionic conductivity, low cost, non-flammability, low toxicity, and ease of handling compared with many organic electrolytes. Nevertheless, the relatively narrow EC stability window of water and the strong dependence of interfacial reactions on electrolyte composition make simultaneous optimization of electrode structure[12] and electrolyte chemistry essential for improving device-level energy and power characteristics [13–17]

Manganese dioxide (MnO_2) has been extensively studied as a transition metal oxide owing to its low cost, environmental friendliness, natural abundance, and the ability to undergo reversible Mn^{3+}/Mn^{4+} pseudocapacitance reactions. It has also high theoretical capacitance and it can be prepared in several polymorphic and nanostructured forms [16, 18]. However, in practice, MnO_2 electrodes only deliver a

fraction of the theoretical capacitance levels due to their poor intrinsic electronic conductivity, slow electron transport through the oxide, limited ion access to internal redox sites and structural or interfacial changes during repeated cycling[18].

Recent studies, therefore, emphasize defect-rich, porous, and electronically connected MnO_2 architectures. Defect engineering and cation doping can modify local bonding, oxygen-vacancy concentration, mixed manganese valence, and charge-transfer kinetics, thereby increasing the number and accessibility of electrochemically active sites[19].

Combining materials such as oxides, metal nanoparticles [20], and sulfide [21, 22] with graphene or its derivatives is a widely used strategy to overcome their conductivity limitation. In MnO_2–graphene hybrids, graphene provides a two-dimensional conductive network, a large interfacial contact area, mechanical support, and short electron-transport pathways, whereas MnO_2 supplies a faradaic contribution that is absent in an ideal carbon-only electric double-layer electrode [19]. The graphene framework can also limit MnO_2 agglomeration and preserve electrolyte-accessible voids between oxide domains and carbon sheets. Nitrogen/sulfur-codoped graphene–MnO_2 films have been developed to improve electronic and ionic transport [7], while rapidly synthesized two-dimensional have demonstrated the suitability of sheet-like interconnected architectures for solid-state symmetric SCs [2]. A sulfonated reduced graphene oxide/graphene oxide/MnO_2 hybrid was also reported as a stable aqueous symmetric SC electrode [1].

In addition to carbon hybridization, electrochemically inactive cations can tune the defect chemistry and electronic structure of MnO_2. Zn^{2+} is particularly relevant because substitutional or interstitial incorporation into the MnO_2 lattice may produce local distortion, alter oxygen coordination, promote oxygen-deficient environments, and influence the Mn^{3+}/Mn^{4+} distribution without acting as the principal redox centre. Zn-doped MnO_2 nanosheets and nanowires have consequently exhibited increased ion-accessible defect populations and improved electrochemical response[23]

An electrolyte-comparison study of Zn-doped δ-MnO_2 nanowires demonstrated that the same doped electrode can exhibit markedly different capacitance and device performance in different aqueous media, with KOH producing a particularly favourable response [23]. Zn doping has also been reported to modulate the spin and electronic states of MnO_2, providing a microscopic basis for improved charge transfer and electrochemical kinetics[4]. These findings support the combination of Zn modification and graphene conduction pathways as a rational strategy for improving MnO_2-based electrodes.

Ionic conductivity, hydrated-ion dimensions and mobility, pH, interfacial adsorption, solvation dynamics and access to redox-active sites are all governed by electrolyte composition. Mobile K^+ and OH^- species in aqueous KOH can result in low solution resistance and fast surface redox processes. Near-neutral Na_2SO_4 offers a more benign chemical environment, but differences in Na^+ hydration and sulfate interactions can modify diffusion and relaxation in confined pores [15].

Beyond heteroatom doping and composite formation, hierarchical porosity and electrolyte selection are therefore central design variables in graphene-based SCs[3]. Direct electrolyte comparison is meaningful only when electrode composition, mass loading, cell configuration, and testing conditions are maintained as consistently as possible. Symmetric cells are useful for such comparisons because identical active materials are employed on both electrodes, simplifying fabrication, mass balancing, and interpretation, although their operating voltage can be narrower than that of optimized asymmetric devices [22].

Despite substantial progress, many MnO_2/graphene (MnO_2/G) studies have focused on three-electrode measurements, asymmetric configurations, a single electrolyte, or undoped oxide–carbon composites. Fewer studies have isolated the effect of electrolyte chemistry in a symmetric two-electrode device containing the same Zn-MnO_2/G active material on both electrodes. In the present work, symmetric Zn-MnO_2/G cells containing KOH electrolyte and Na_2SO_4 electrolyte were denoted GMK and GMN, respectively. Scanning electron microscopy with energy-dispersive X-ray spectroscopy (SEM/EDS), X-ray diffraction (XRD), X-ray photoelectron spectroscopy (XPS), and nitrogen adsorption–desorption analysis using the Barrett–Joyner–Halenda (BJH) method were used to examine morphology, elemental distribution, crystal structure, surface chemical states, and pore characteristics. Cyclic voltammetry (CV), galvanostatic charge–discharge (GCD), electrochemical impedance spectroscopy (EIS), and Bode-phase analysis were used to correlate electrolyte-dependent ion transport and interfacial relaxation with device-level charge storage. By retaining the same electrode material and symmetric architecture, this study aimed to clarify how alkaline and near-neutral aqueous environments influence the electrochemical utilization of porous Zn-MnO_2/G electrodes.

2. Experimental Section

Materials

Graphene, manganese oxide, metallic zinc, KOH, Na_2SO_4, acetylene black as the conductive additive, poly(vinylidene fluoride) (PVDF) as the binder, N-methyl-2-pyrrolidone (NMP) as the solvent, and stainless-steel current collectors were used for composite and electrode preparation.

Synthesis of Zn-MnO_2/G Composite

The $ZnMnO_2$/G composite was synthesized by a simple acetone-assisted continuous mixing method using graphene, manganese oxide and metallic zinc as raw materials. At first, the graphene powder was dispersed in acetone with continuous magnetic stirring to form a uniform suspension. Acetone was used as a dispersion medium to improve the wetting of the surface of graphene and the homogeneous mixture of the solid components. The suspension was sonicated further to reduce the agglomeration of graphene sheets and to expose more surface sites for attachment of manganese oxide particles. Once a uniform dispersion of graphene was achieved, the required amount of manganese oxide was added

gradually with continuous stirring. The mixture was stirred well to allow a uniform distribution of manganese oxide on the graphene framework.

Then the graphene-manganese oxide suspension was gradually treated with metallic zinc powder under continuous stirring. The mixture was stirred continuously to have intimate contact of the graphene, manganese oxide and zinc. In the process, graphene is used as a conductive support and zinc is incorporated into the manganese oxide/graphene matrix, yielding a zinc-modified MnO_2/graphene composite. The mixture was stirred constantly and then heated to 100°C for 3 h to evaporate acetone. The heating step was also beneficial in respect to the evaporation of the solvent and increased interactions between the graphene, manganese oxide and zinc components. The dried product was carefully powdered in an agate mortar to a fine, homogeneous powder.

Fabrication of Electrodes and Assembly of Symmetric Cells

The Zn-MnO_2/G active composite was mixed with acetylene black and PVDF to prepare a homogeneous slurry in NMP. The slurry was coated on identical stainless steel current collectors and dried to remove the solvent. A symmetric two-electrode cell was assembled using Zn-MnO_2/G as two electrodes, with two electrodes having similar active material loading. Electrolytes for comparative evaluation were aqueous KOH and Na_2SO_4. The symmetric device based on KOH was denoted as GMK and the symmetric device based on Na_2SO_4 was denoted as GMN. This setup allowed direct comparison of electrolyte effects without changing electrode composition.

Material Characterization

Surface morphology and element distribution were studied by SEM/EDS. The surface chemical states were analyzed by XPS, and the crystalline features were analyzed by XRD with Cu Kα radiation. The mesopore-size distribution, the cumulative pore volume and the pore surface area were evaluated by nitrogen adsorption–desorption measurements and BJH analysis.

Electrochemical Measurements and Calculations

CV, GCD, EIS and Bode-phase measurements were performed on a symmetric two-electrode configuration using KOH and Na_2SO_4 electrolytes. The KOH and Na_2SO_4 cells were designated as GMK and GMN, respectively. Measurements at the device level were made in a 0–1.0 V window. The CV curves were measured at the scan rates of 5–50 mV s^{-1} and the GCD curves were measured at the current densities of 0.1–0.5 A g − 1. The EIS measurements were carried out within the frequency range studied by applying a small-amplitude AC perturbation at the open circuit potential.

3. Results and Discussion

3.1. Morphology and Elemental Distribution

As shown in the SEM image and elemental maps (Figure.1), the composite has a rough interconnected morphology with oxide domains in a graphene-rich matrix. The carbon map is mostly continuous, consistent with a conductive graphene network.

The oxygen and manganese maps reveal the presence of manganese oxide, while the EDS spectrum confirms the expected elemental signatures of the composite. For a Zn MnO_2/graphene electrode, this type of morphology is desirable because graphene provides electron-transport pathways, whereas the oxide phase contributes surface and near-surface redox activity [7].

The low-magnification SEM image of the Zn-MnO_2/G composite (Fig. 1(a)) showed a rough, crumpled, and sheet-like morphology. The graphene sheets appear as stacked and wrinkled layers, providing a large surface area and conductive network for charge transport. The irregularly distributed particulate features on the graphene surface indicate the formation/deposition of oxide species on the graphene framework. The EDS elemental mapping (Fig. 1(b)) of carbon obtained from the mapped region, showed a continuous and dominant carbon distribution throughout the scanned area. This confirms the presence of graphene as the major matrix/supporting phase in the composite. Figure 1(c) shows EDS elemental mapping of manganese (Mn) showing the distribution of Mn-containing regions over the graphene surface. The Mn signal appears as scattered bright domains, indicating that MnO_2 particles are distributed over the graphene sheets rather than forming a completely continuous layer. The EDS elemental mapping of oxygen (Fig. 1(d)) showed oxygen-rich regions across the composite.

The oxygen distribution coincides with the Mn-rich regions which support the formation of manganese oxide species. The oxygen signal also suggests the presence of surface oxygen functional groups associated with graphene and oxide phases. Figure 1(e) shows the SEM image of the selected region for EDS spectral analysis. The image has confirmed the composite morphology where the layered graphene sheets are decorated by irregular oxide particles. The corresponding EDS spectrum was taken of this SEM region. Figure 1(f) shows EDS spectrum corresponding to the area shown in (e). The spectrum confirms the presence of C, O, Mn and Zn in the composite. The strong carbon peak is from the graphene framework, and the Mn and O peaks confirm the MnO_2 phase. The Zn signal confirms the successful incorporation of Zn into the MnO_2/graphene composite. The source of minor signals could be the sample holder, conductive tape and the instrumentation background. To summarize, the SEM–EDS results verify the formation of Zn-MnO_2/G composite with oxide particles dispersed on the graphene network.

The N_2 adsorption–desorption isotherm (Fig. 2a) and BJH adsorption pore-size distribution (Fig. 2b) indicated electrolyte-accessible mesoporosity in the Zn-MnO_2/G composite. The adsorption–desorption hysteresis was consistent with mesopore filling and capillary condensation. The steep uptake at high relative pressure was attributed to larger mesopores and interparticle voids between graphene sheets and oxide domains; macroporosity was not assigned because conventional N_2 adsorption and BJH analysis do not reliably quantify macropores. BJH analysis yielded a cumulative pore volume of 4.53328 × 10^{-2} cm^3 g^{-1} and a cumulative pore surface area of approximately 12.996 m^2 g^{-1}. The differential pore-

volume distribution reached its maximum at a pore radius of 1.69 nm, corresponding to a pore width of approximately 3.38 nm, and decreased with increasing pore radius. The mesoporous texture can promote electrolyte penetration and shorten ion-transport pathways to Mn redox-active sites[7] .

The high-resolution XPS spectra of the Zn- MnO_2/G composite were deconvoluted to identify the chemical states and bonding environment of the constituent elements. The survey of core-level regions confirms the presence of C, O, Mn, and Zn, supporting the successful formation of the Zn-MnO_2/G composite. The high-resolution C 1s spectrum showed a broad asymmetric envelope, which was deconvoluted into several chemically distinct carbon-related components.

The peak at ~ 284.5 eV is attributed to C–C/C = C bonds associated with the graphitic carbon framework of graphene. The components observed at slightly higher binding energies, around 285.3–286.0 eV, correspond to carbon-oxygen bonds, such as C-O and C-OH groups. Additional peaks at higher binding energies (ca. 286.5–287.5 eV) could be assigned to C = O and O–C = O functionalities[24]. These oxygen-containing functional groups imply partial oxidation/functionalization of the graphene surface, which can better anchor MnO_2 and Zn species. This interfacial bonding is beneficial for preventing particle agglomeration and enhancing the electronic coupling between graphene and the oxide phase [23]. The low binding energy shoulder could also be due to defect rich or sp^2/sp^3 hybridized carbon environments. Overall, the spectrum of C_{1s} confirms the presence of graphene with surface oxygen functionalities that facilitate the formation of a well-integrated composite structure. The broad O $_{1s}$ spectrum with multiple oxygen environments demonstrates the presence of lattice oxygen, defect-related oxygen, and surface-adsorbed oxygen species.

The lower-binding-energy component near 529.5–530.2 eV can be assigned to lattice oxygen (Mn–O/Mn–O–Mn) in manganese oxide. The peaks located around 531.0–532.0 eV are generally associated with oxygen vacancies, hydroxyl groups, or defect-related oxygen species. These oxygen-deficient sites can contribute to improved electrochemical activity by providing additional active sites and enhancing ion adsorption during charge storage [25]. The higher-binding-energy components near 533.0–534.5 eV can be attributed to surface-adsorbed oxygen, water molecules, carbonate-like species, or oxygen-containing functional groups on graphene. The presence of hydroxyl/adsorbed oxygen species is important for aqueous electrochemical charge storage because these surface sites can participate in electrolyte-assisted redox and adsorption processes in both KOH and Na_2SO_4 media. Therefore, the O 1s spectrum supports the formation of Mn–O bonding, as well as defect-rich and surface-active oxygen species, which are favorable for pseudocapacitive charge storage. The Mn 2p spectrum shows the characteristic spin–orbit doublet corresponding to Mn $2p_3/_2$ and Mn $2p_1/_2$. The main Mn $2p_3/_2$ peak appears in the range of approximately 640–645 eV, while the Mn $2p_1/_2$ peak is observed around 652–656 eV. The separation between these two peaks confirms the presence of manganese oxide. The deconvoluted components indicate the coexistence of multiple Mn oxidation states, primarily Mn^{3+} and Mn^{4+}, which is characteristic of non-stoichiometric MnO_2-based materials. The lower-binding-energy components can be related to Mn^{3+} species, whereas the higher-binding-energy components are generally associated with Mn^{4+} species. The coexistence of Mn^{3+}/Mn^{4+} redox couple is highly beneficial

for supercapacitor applications because reversible transitions between these oxidation states contribute to pseudocapacitive charge storage. In addition, the presence of mixed valence states suggests the formation of defect sites and oxygen vacancies, which can enhance electronic conductivity and promote faster surface redox reactions [25]. Thus, the Mn 2p spectrum confirms the formation of electrochemically active manganese oxide in the composite. The Zn 2p spectrum shows two major spin–orbit components corresponding to Zn $2p_3/_2$ and Zn $2p_1/_2$, located approximately near 1021–1023 eV and 1044–1046 eV, respectively. The energy separation between Zn $2p_3/_2$ and Zn $2p_1/_2$ is consistent with Zn in the Zn^{2+} oxidation state. The deconvolution of the Zn 2p region suggests that Zn is chemically incorporated within the oxide environment rather than present only as metallic Zn. The presence of Zn^{2+} may induce local structural distortion and generate additional defect sites or oxygen vacancies in the MnO_2 lattice. Such Zn-induced defect formation can improve electrochemical performance by increasing the number of active sites, enhancing electrolyte accessibility, and facilitating charge-transfer kinetics [25]. The successful detection of Zn 2p peaks confirms the incorporation of Zn into the MnO_2/graphene composite. Overall, the XPS results confirm the formation of a Zn-doped MnO_2/graphene composite containing graphitic carbon, oxygen-functionalized graphene, mixed-valence manganese oxide, and Zn^{2+} species. The coexistence of Mn^{3+}/Mn^{4+} redox centers, oxygen vacancies, surface hydroxyl/adsorbed oxygen species, and conductive graphene support is expected to enhance the pseudocapacitive behavior of the electrode [25][7].

The oxygen functionalized graphene surface favors the anchoring of oxides and the incorporation of Zn can modify the electronic structure and defect chemistry of MnO_2. These features synergistically improve the ion transport, charge-transfer kinetics and electrochemical utilization of Mn redox-active sites in aqueous electrolytes such as KOH and Na_2SO4.

The XRD pattern (Fig. 4) contained a strong reflection in the graphitic/oxide region and several sharper reflections, confirming that the composite included crystalline constituents in addition to the graphene-rich phase. Because the embedded pattern was not accompanied by the original diffraction data or a validated phase-reference file, crystallographic planes and individual Zn-containing phases were not assigned. Definitive phase identification requires background correction, extraction of the experimental 2θ peak positions, and comparison with appropriate reference patterns for the relevant MnO_2 polymorph, graphene, and possible residual Zn-containing phases.

Figure 5(a,b) shows CV curves of the symmetric GMK and GMN devices recorded at scan rates of 5–50 mV s^{-1}. The curves displayed stable current responses within the 0–1.0 V device window. Their quasi-rectangular shapes with broad redox contributions indicated hybrid charge storage involving electric double-layer charging on graphene and surface redox reactions of MnO_2. Because the active electrode material was identical, both cells exhibited the same general pseudocapacitive character; however, electrolyte identity affected current response, polarization, and rate behaviour [26]. The KOH environment facilitated OH^--assisted surface processes and access to Mn redox sites, whereas hydrated Na^+ transport and sulfate interactions in near-neutral Na_2SO_4 solutions led to distinct transport and relaxation characteristics [15, 16].

The specific capacitance, energy density, and power density of the symmetric supercapacitor devices were calculated using the following equations:

$$C_s = \frac{4I\Delta t}{m_{total}\Delta V} \quad (1)$$

$$E = \frac{C_s(\Delta V)^2}{2(3.6)} \quad (2)$$

$$P = \frac{E(3600)}{\Delta t} \quad (3)$$

Here, C_s is the specific capacitance (F/ g), I is the discharge current (A), Δt is the discharge time (s), m_{total} is the total active mass of both electrodes (g), ΔV is the voltage window (V), E is the energy density (Wh kg⁻¹), and P is the power density (W kg⁻¹).

The energy density and power density of the symmetric GMK and GMN supercapacitor devices were calculated from the GCD curves using the specific capacitance values obtained at different current densities using equations (1)-(3). GMK, measured in KOH electrolyte, delivered a higher energy density than GMN measured in Na_2SO_4 electrolyte. At 0.1 A g⁻¹, GMK exhibited an energy density of approximately 0.84 Wh kg⁻¹ with a power density of about 200 W kg⁻¹. With increasing current density, the energy density gradually decreased to approximately 0.58 Wh kg⁻¹ at 0.5 A g⁻¹, while the power density increased to about 1000 W kg⁻¹.

Such behavior is typical for supercapacitors, where at lower current density the diffusion of ions and utilization of electroactive Mn redox centers is more complete, while at higher current density the power output is higher but the charge-storage capability is lower [27, 28].

The maximum energy density of the GMN device was ~ 0.57 Wh kg^{-1} at 0.025 A g^{-1} with a power density of ~ 50 W kg^{-1}. At higher current densities, the energy density was decreased by 0.33 Wh kg^{-1} and the power density was increased to ~ 600 W kg^{-1}. The relatively low energy density of GMN means less efficient charge storage in Na_2SO_4, which could be linked to different Na^+ transport, sulfate-ion interaction, near-neutral electrolyte chemistry and lower accessibility of electroactive Mn sites under fast charge-discharge conditions. In contrast, the KOH electrolyte of GMK provides a more favorable K^+/OH^- transport environment, improving electrolyte penetration, charge-transfer kinetics and utilization of the Mn redox centers.

Therefore, the GMK device demonstrates superior energy-storage performance compared with GMN .

The GCD profiles measured at 0.1, 0.2, 0.3 and 0.5 A g^{-1} demonstrate reversible charge storage in the 0–1.0 V window.

As expected for MnO_2 based pseudocapacitive electrode, the curves are not perfectly triangular, due to potential-dependent redox reactions that change the charge-discharge slope[26]. The discharge time decreases as current density increases, supporting rate dependent capacitance. The GMK cell shows a relatively good charge-discharge profile in line with reduced impedance and a stronger capacitive phase response in KOH. The reversibility is also observed for the GMN cell but the electrochemical signatures indicate that different ion transport and charge transfer conditions are created by Na_2SO_4[14].

The Nyquist plots of Zn-MnO_2/G electrodes in KOH and Na_2SO_4 electrolytes are shown in Fig. 6 and were used to analyze the EIS responses. Both spectra showed a small depressed semicircle in the high frequency region followed by a linear inclined response at lower frequencies indicating the contribution of charge transfer resistance and diffusion influenced capacitive behavior[15].

The symmetric electrolyte-dependent devices exhibit capacitive and resistive behavior which is further confirmed by the Nyquist analysis. The high frequency intercept is equivalent to the series resistance, including electrolyte resistance, intrinsic electrode resistance and contact resistance. In the high to middle frequency region, the semicircle or depressed arc is attributed to the charge-transfer resistance of the electrode/electrolyte interface[15].

GMK displays a smaller high-frequency arc and a steeper low-frequency branch than GMN, suggesting lower interfacial resistance and more efficient capacitive ion storage in KOH. The relatively larger impedance of GMN implies slower ion transport and/or less favorable charge-transfer kinetics in Na_2SO_4 for the same electrode configuration[15].

The experimental data were fitted using the equivalent circuit $R_s + (R_{ct} \parallel CPE_1) + CPE_2$, where $R_s$represents the solution/internal resistance, R_{ct}corresponds to the charge-transfer resistance at the electrode–electrolyte interface, and the constant phase elements account for non-ideal capacitive behaviour arising from surface roughness, porosity, and distributed ion transport pathways.The equivalent series resistance was obtained from the high-frequency intercept on the Z' axis. The charge-transfer resistance was estimated from the diameter of the high-frequency semicircle. A smaller semicircle and a steeper low-frequency line indicate lower interfacial resistance and better capacitive ion diffusion[15].

Comparison to the GMN electrode, the GMK electrode exhibited a lower overall impedance range and a steeper low-frequency response. This suggests improved transport of electrolyte ions and enhanced capacitive response in the latter. The more vertical low frequency line of GMK indicates faster ion diffusion and better accessibility of electroactive sites in the porous Zn–MnO_2/G electrode structure. While the GMN exhibited a more extensive impedance response, suggesting a relatively slower ion migration and a higher diffusion resistance. The good overlap between the experimental curves and the fitted curves confirmed that the adopted equivalent circuit model is suitable for describing the charge-transfer at the interface and the ion transport processes in the both electrolytes. The fitted EIS equivalent-circuit parameters of electrodes in KOH and Na_2SO_4 electrolytes using the circuit Rs + (Rct

||CPE 1) + CPE 2 are summarized in Table 1, where R s is the series resistance, R ct is the charge-transfer resistance, and CPE is the constant phase element.

Table 1
Fitted EIS equivalent circuit parameters of Zn–MnO_2 /G electrodes in KOH and Na_2SO_4 electrolytes based on the circuit R s + (R ct || CPE 1) + CPE 2 .

Parameter	**GMK — KOH electrolyte**	**GMN — Na_2SO_4 electrolyte**
R (series resistance)	0.1788 Ω	1.7700 Ω
Rct (charge-transfer resistance)	9.4575 Ω	6.9773 Ω
CPE_1 Q	0.00095	3.4×10^{-5}
CPE_1 n	0.461	0.578
CPE_1 phase angle (n × 90°)	41.4°	52.1°
CPE_2 Q	0.0386	0.00781
CPE_2 n	0.753	0.623
CPE_2 phase angle (n × 90°)	67.7°	56.1°

Figure. 7 shows Bode phase-angle plots of Zn–MnO_2/G electrodes measured in KOH electrolyte (GMK) and Na_2SO_4 electrolyte (GMN). The more negative low-frequency phase angle of GMK indicates higher capacitive behavior and better ion accessibility in KOH. The deviation from the ideal − 90° phase angle is indicative of non-ideal capacitive behavior due to porous electrode structure, interfacial resistance and distributed ion-diffusion processes.

The Bode-phase plot shows the frequency-dependent response of the symmetric devices in the two electrolytes. Ideal capacitive behavior is indicated by a phase angle close to -90 degrees at low frequency, while deviations from − 90 degrees indicate resistive, diffusion-controlled or pseudocapacitive contributions [15]. The capacitive phase response is more pronounced in the low-to-intermediate frequency range in GMK (measured in KOH) than in GMN (measured in Na_2SO_4). This shows that the KOH based cell has a faster electrolyte assisted relaxation and more favorable ion/electron transport. The different relaxation profiles confirm the strong influence of the electrolyte environment on interfacial kinetics in Zn-MnO_2/G electrodes[15].

The characteristic relaxation time of the device can be estimated from the Bode plot using τ0 = 1/f0, where f0 is the frequency at which the phase angle reaches − 45°. A lower τ0 correlates with a rapid capacitive response and an accelerated ion/electron transport across the electrode-electrolyte interface[15].

To further investigate the frequency-dependent capacitive behaviors of the Zn–MnO_2/G electrodes, we present the Bode phase-angle plots of GMK and GMN in Fig. 7. The phase angles of both electrodes are

negative over the measured frequency range confirming the existence of capacitive charge-storage behavior along with resistive contributions. GMK has a phase angle of ~ − 55° at low frequency, where electrolyte ions have enough time to penetrate the porous electrode structure, while GMN has ~ − 50°. GMK exhibits a slightly more negative phase angle, indicating a larger capacitive contribution in KOH electrolyte.

The phase angle slowly moves toward less negative values with increasing frequency, indicating the change from ion diffusion-controlled capacitive behavior to more resistive behavior. The quicker phase transition of GMK indicates a quicker electrochemical response and simpler ion transportation in KOH electrolyte. Conversely, GMN shows a broader frequency-dependent response which implies more distributed relaxation processes in Na_2SO_4 .

The deviation of the phase angle from the ideal capacitor value of − 90° confirms the non-ideal capacitive nature of the electrodes, which can be attributed to electrode porosity, surface roughness, charge-transfer resistance, and heterogeneous ion diffusion pathways.

Overall, the Bode phase response supports the Nyquist analysis, confirming that the electrolyte strongly influences the ion-transport and charge-storage behaviour of the Zn–MnO_2/G electrode. The more negative low-frequency phase angle of GMK indicates comparatively better capacitive behaviour in KOH electrolyte.

The variation in energy density with current density was analysed using an empirical physical rate-capability fitting model,

$$E = E_0 - bJ \text{ (4) ...}$$

where $E$is the fitted energy density, $J$is the applied current density, E_0represents the extrapolated low-current energy density, and $b$is the rate-loss coefficient. The fitting was implemented using a Python-based computational curve-fitting approach. The experimentally calculated energy-density values were fitted to the above empirical relation, and the parameters $E_0$and $b$were optimized by least-squares minimization. The fitting was performed independently for each electrolyte so that separate rate-loss coefficients could be obtained for the KOH- and Na_2SO_4 based symmetric supercapacitors.

For both GMK and GMN, the experimental energy density decreased with increasing current density. At relatively low current density, the longer discharge time allows electrolyte ions to penetrate the accessible mesoporous network and interact with a larger fraction of the Mn redox-active sites. This results in higher electrochemical utilization, higher specific capacitance, and therefore higher energy density. With increasing current density, the charge–discharge time shortens, thereby restricting ion diffusion through the internal pore network and reducing the effective utilization of the active surface. Consequently, the energy density decreases progressively as current density increases. This behaviour is typical of porous pseudocapacitive electrodes, where the measured charge-storage response depends strongly on the timescale of ion transport and surface redox reactions.

In the present fitting model, the rate-loss coefficient $b$provides a simple quantitative measure of the decrease in energy density per unit increase in current density. A smaller $b$value indicates that the device can retain energy density more effectively at higher current density, whereas a larger $b$value indicates stronger rate-induced energy loss. Therefore, $b$reflects the combined influence of ion-transport limitation, interfacial polarization, incomplete utilization of electroactive sites, and resistance-related losses under fast charge–discharge conditions.

The KOH-based GMK device exhibits higher energy-density retention than the Na_2SO_4-based GMN device over the investigated current-density range. The fitted rate-loss coefficient for KOH is smaller than that for Na_2SO_4 confirming that KOH provides more favourable charge-storage kinetics under high-current operation. This behaviour can be associated with the favourable ion-transport characteristics of the KOH electrolyte, efficient OH^- assisted surface redox reactions involving manganese oxide, and lower interfacial resistance. In contrast, the Na_2SO_4 based GMN device exhibits a larger rate-loss coefficient, suggesting stronger ion-transport limitation and less effective utilization of the electroactive sites at higher current density.

Overall, the empirical physical rate-capability fitting confirms the experimentally observed decrease in energy density with increasing current density and highlights the superior rate capability of the KOH-based GMK device compared with the Na_2SO_4 based GMN device. The lower rate-loss coefficient in KOH indicates better energy-density retention, more efficient electrochemical utilization, and reduced transport limitation during faster charge–discharge operation. Thus, the fitting analysis supports the conclusion that the electrolyte plays a major role in controlling the rate-dependent energy-storage behaviour of the Zn-doped MnO_2/G symmetric supercapacitor.

4. Conclusions

A Zn-MnO_2/G composite electrode was evaluated in symmetric supercapacitors using aqueous KOH and Na_2SO_4 as electrolytes. Various characterization techniques confirmed the formation of a graphene-supported Zn-modified manganese oxide composite with a rough, interconnected oxide morphology. Nitrogen adsorption–desorption and BJH analyses revealed a mesoporous texture with a cumulative pore volume of 0.0453 $cm^3\ g^{-1}$, a pore surface area of ~ 13.0 $m^2\ g^{-1}$, and a dominant pore width of approximately 3.38 nm. Electrochemical studies showed the stable capacitive behaviour with the operating window of 0– 1.0 V, quasi-rectangular CV profiles, pseudocapacitive GCD responses, good impedance properties and capacitive Bode-phase behavior. In the Zn-MnO_2/G symmetric-cell system studied, GMK showed superior energy density retention and rate capability than GMN. This enhancement was attributed to the synergistic effect of improved ion transportation, reduced interfacial resistance, and increased utilization of Mn redox-active sites in KOH. The results thus demonstrate that the electrolyte chemistry couples to the pore structure, interfacial properties and redox chemistry of the electrode rather than being a universally independent performance variable. Further optimization of the

Zn content, electrode mass loading, long-term cycling stability and direct comparison of the composite with undoped MnO_2/graphene electrodes will be the subject of future work.

Declarations

Author Contribution

K.N. , Elsa, Riswana wrote the main manuscript text and Vipin Das V,C.S Preenu prepared figures . All authors reviewed the manuscript. J R R,AG did complete supervision and editing of the manuscript, Sandhya Karunakaran helped for experimental studies

Funding Declaration

This research received no specific grant from any funding agency in the public, commercial, or not-for-profit sectors.

References

1. Gurunathan K, Tchekep AGK, Arunkumar M, Pattanayak DK, Sathish M (2026) Bifunctional Electrochemical Behavior of S-rGO@GO/MnO_2 for Advanced Supercapacitor and Lithium-Ion Hybrid Capacitor. Batter Supercaps 9:e202500683. https://doi.org/10.1002/batt.202500683
2. Nanda OP, Chahal S, Badhulika S (2025) Rapid and sustainable microwave synthesis of two-dimensional (2D) MnO_2-Graphene hybrid nanostructures for high-efficiency solid-state symmetric supercapacitors with superior cycling stability. Mater Chem Phys 338:130627. https://doi.org/10.1016/j.matchemphys.2025.130627
3. Sagar P, Hamdani IR, Levato T, Giannini V, Das G (2026) Graphene and its derivatives in supercapacitors: A comparative review. Mater Adv 7:83–108. https://doi.org/10.1039/D5MA01017A
4. Liu J, Zhang X, Wu X, Hai J, Li X, Feng R, Gao Y (2026) Spin State Modulation of MnO_2 by Zn-Doping for Enhanced Supercapacitor and Hydrogen Evolution, EChem 2. 5. https://doi.org/10.53941/echem.2026.100005
5. Augustyn V, Simon P, Dunn B (2014) Pseudocapacitive oxide materials for high-rate electrochemical energy storage. Energy Environ Sci 7:1597–1614. https://doi.org/10.1039/c3ee44164d
6. Chen GZ (2017) Supercapacitor and supercapattery as emerging electrochemical energy stores. Int Mater Rev 62:173–202. https://doi.org/10.1080/09506608.2016.1240914
7. Raei MJ, Trifkovic M, Roberts EPL, Natale G (2025) One-Step Synthesis of Nitrogen/Sulfur Codoped Graphene/MnO_2 Film as a High-Performance Supercapacitor, ACS Appl. Energy Mater 8:10822–10832. https://doi.org/10.1021/acsaem.5c00530
8. Davidi E, Xue X, Li Y (2026) Electrodeposited manganese dioxide for pseudocapacitors and batteries. Inorg Chem Front 13:1268–1290. https://doi.org/10.1039/d5qi01411e

9. Arya Nair JS, Anjana PM, Dais E, Dhrishya V, Rakhi RB, Sandhya KY (2026) Synergistic Effect in an Edge-Functionalized Water-Processable Graphene With MoS_2 Hollow Nanoflowers for a High-Performance Supercapacitor Electrodes. Batter Supercaps 9:e70297. https://doi.org/10.1002/batt.70297
10. Dais E, Vijayanandan D, Josily J, Karunakaran Yesodha S (2026) Plastic Waste-Upcycled Nanoporous Carbon-MoS_2 Composite for High-Performance Supercapacitor Electrode-Enriched Pseudocapacitive Behavior via Interfacial Bonds. ACS Appl Electron Mater 8:7395–7406. https://doi.org/10.1021/ACSAELM.6C00965
11. Rani JR, Thangavel R, Oh SI, Lee YS, Jang JH (2019) An ultra-high-energy density supercapacitor; fabrication based on thiol-functionalized graphene oxide scrolls. Nanomaterials 9. https://doi.org/10.3390/nano9020148
12. Arya Nair JS, Chirag S, Sandhya KY (2021) A promising rosy future for supercapacitors: Suitability of MoS_2 hollow nanoroses for supercapacitor electrodes. Int J Mater Res 112:945–948. https://doi.org/10.3139/146.111964
13. Salanne M, Rotenberg B, Naoi K, Kaneko K, Taberna P-L, Grey CP, Dunn B, Simon P (2016) Efficient storage mechanisms for building better supercapacitors. Nat Energy 1:16070. https://doi.org/10.1038/nenergy.2016.70
14. González A, Goikolea E, Barrena JA, Mysyk R (2016) Review on supercapacitors: Technologies and materials, Renew. Sustain Energy Rev 58:1189–1206. https://doi.org/10.1016/j.rser.2015.12.249
15. Soltani H, Bahiraei H, Ghasemi S, Hashempour M (2025) Rate capability and electrolyte concentration: Tuning MnO_2 supercapacitor electrodes through electrodeposition parameters. Heliyon 11:e41427. https://doi.org/10.1016/j.heliyon.2024.e41427
16. Kore AE, Kore EK, Gavande SS, Molane AC, Mulik RN, Krishnan K, Patil VB (2025) Effect of different electrolytes on the efficient performance of δ-MnO_2 electrode for supercapacitor applications. Mater Sci Eng B 313:117992. https://doi.org/10.1016/j.mseb.2025.117992
17. Rani JR, Das NC, Kim M, Thangavel R, Kim ST, Lee YS, Jang J-H (2023) Realizing high energy density supercapacitors assisted by light-induced charging. J Power Sources 576:233197. https://doi.org/https://doi.org/10.1016/j.jpowsour.2023.233197
18. Devaraj S, Munichandraiah N (2008) Effect of Crystallographic Structure of MnO_2 on Its Electrochemical Capacitance Properties. J Phys Chem C 112:4406–4417. https://doi.org/10.1021/jp7108785
19. Zhang X, Zhang F, Wei D, Cai Z, Song Y, Wang X (2023) Design and synthesis of K-doped tremella-like δ-MnO_2 for high-performance supercapacitor. J Energy Storage 72:108468. https://doi.org/10.1016/j.est.2023.108468
20. Yang K, Cho K, Yoon DS, Kim S (2017) Bendable solid-state supercapacitors with Au nanoparticle-embedded graphene hydrogel films. Sci Rep 7:40163. https://doi.org/10.1038/srep40163

21. Arya Nair JS, Saisree S, Sandhya KY (2022) Picomolar level electrochemical detection of hydroquinone, catechol and resorcinol simultaneously using a MoS2 nano-flower decorated graphene. Analyst 147:2966–2979. https://doi.org/10.1039/d2an00531j
22. Arya Nair JS, Saisree S, Sandhya KY (2023) Trace-Level Detection of Pb(II) and Cd(II) Aided by MoS_2 Nanoflowers and Graphene Nanosheet Combination. ACS Appl Eng Mater 1:924–935. https://doi.org/10.1021/acsaenm.2c00191
23. Kore AE, Kore EK, Gavande SS, Molane AC, Nimbalkar TM, Mulik RN, Selvaraj M, Assiri MA, Patil VB (2025) Impact of various aqueous electrolytes on the electrochemical performance of Zinc-doped δ-MnO_2 nanowires as electrode material for supercapacitor device applications. J Alloys Compd 1042:184116. https://doi.org/10.1016/j.jallcom.2025.184116
24. Rani JR, Thangavel R, Oh SI, Woo JM, Chandra Das N, Kim SY, Lee YS, Jang JH (2017) High Volumetric Energy Density Hybrid Supercapacitors Based on Reduced Graphene Oxide Scrolls, ACS Appl. Mater Interfaces 9:22398–22407. https://doi.org/10.1021/acsami.7b03299
25. Faiz F, Wu J, Tayyab M, Rauf S, Shafqat Z, Asghar A, Ahmad M, Hu J, Alanazi N, Faiz Y, Zhao X, Wu J (2026) Boosting aqueous supercapacitor performance by defect-engineered Co-MnO_2 nanoparticles: A combined experimental and DFT investigation. J Alloys Compd 1075:189155. https://doi.org/10.1016/j.jallcom.2026.189155
26. Patil PH, Jadhav SA (2024) Manganese dioxide (MnO_2) and biomass-derived carbon-based electroactive composite materials for supercapacitor applications. RSC Appl Interfaces 1:624–647. https://doi.org/https://doi.org/10.1039/d4lf00085d
27. Yan J, Wang Q, Wei T, Fan Z (2014) Recent Advances in Design and Fabrication of Electrochemical Supercapacitors with High Energy Densities. Adv Energy Mater 4:1300816. https://doi.org/10.1002/aenm.201300816
28. Conway BE (1999) Electrochemical Supercapacitors, Scientific Fundamentals and Technological Applications

Figures

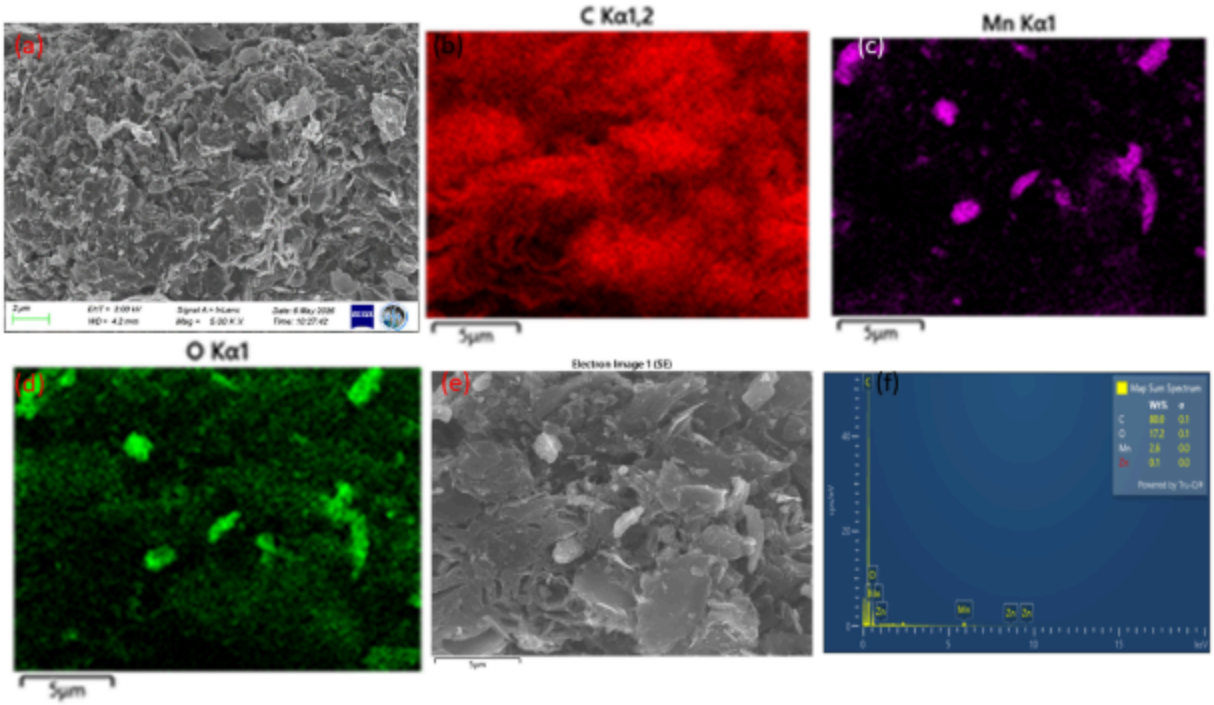
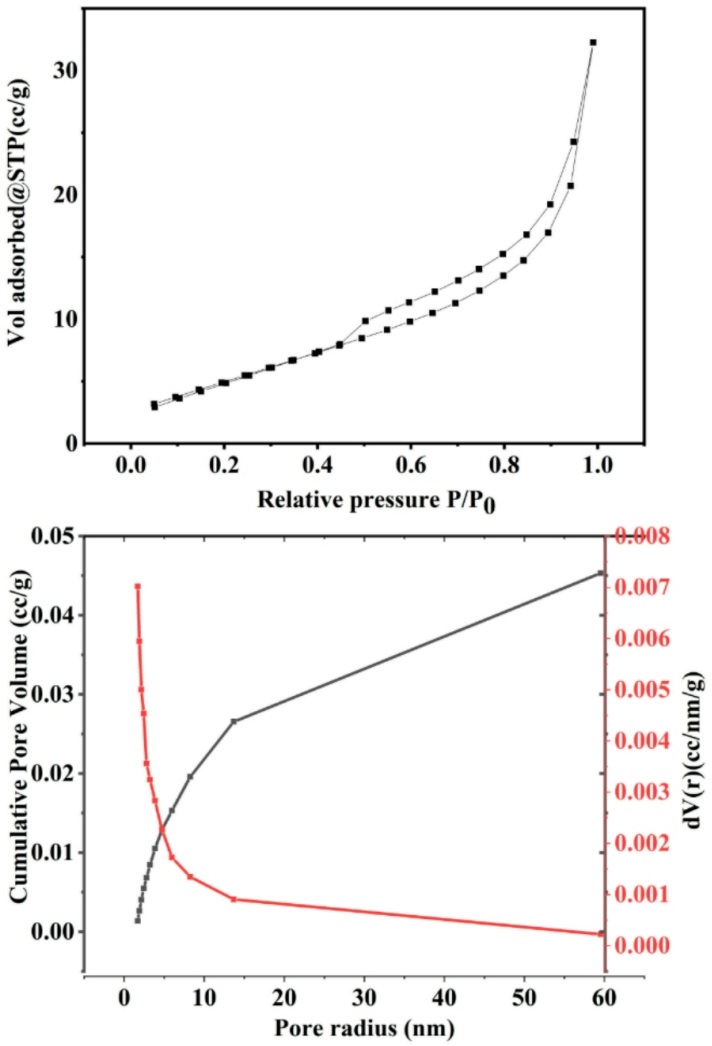


Figure 1

Morphological and elemental analysis of the Zn- MnO_2/G composite. (a) SEM image showing the rough, wrinkled, and sheet-like morphology of the graphene-based composite with oxide particles distributed over the surface. (b–d) EDS elemental mapping images showing the distribution of C, Mn, and O, respectively, confirming the coexistence of graphene and manganese oxide phases in the composite. (e) SEM image of the selected region used for EDS analysis. (f) Corresponding EDS spectrum collected from the SEM region shown in (e)



(a)

Figure 2

(a) N_2 adsorption–desorption isotherm and (b) BJH adsorption pore-size distribution of the Zn-MnO_2/G composite. The material exhibited a cumulative BJH pore volume of 0.0453 $cm^3\ g^{-1}$, a pore surface area of approximately 13.0 $m^2\ g^{-1}$, and a dominant pore width of approximately 3.38 nm.

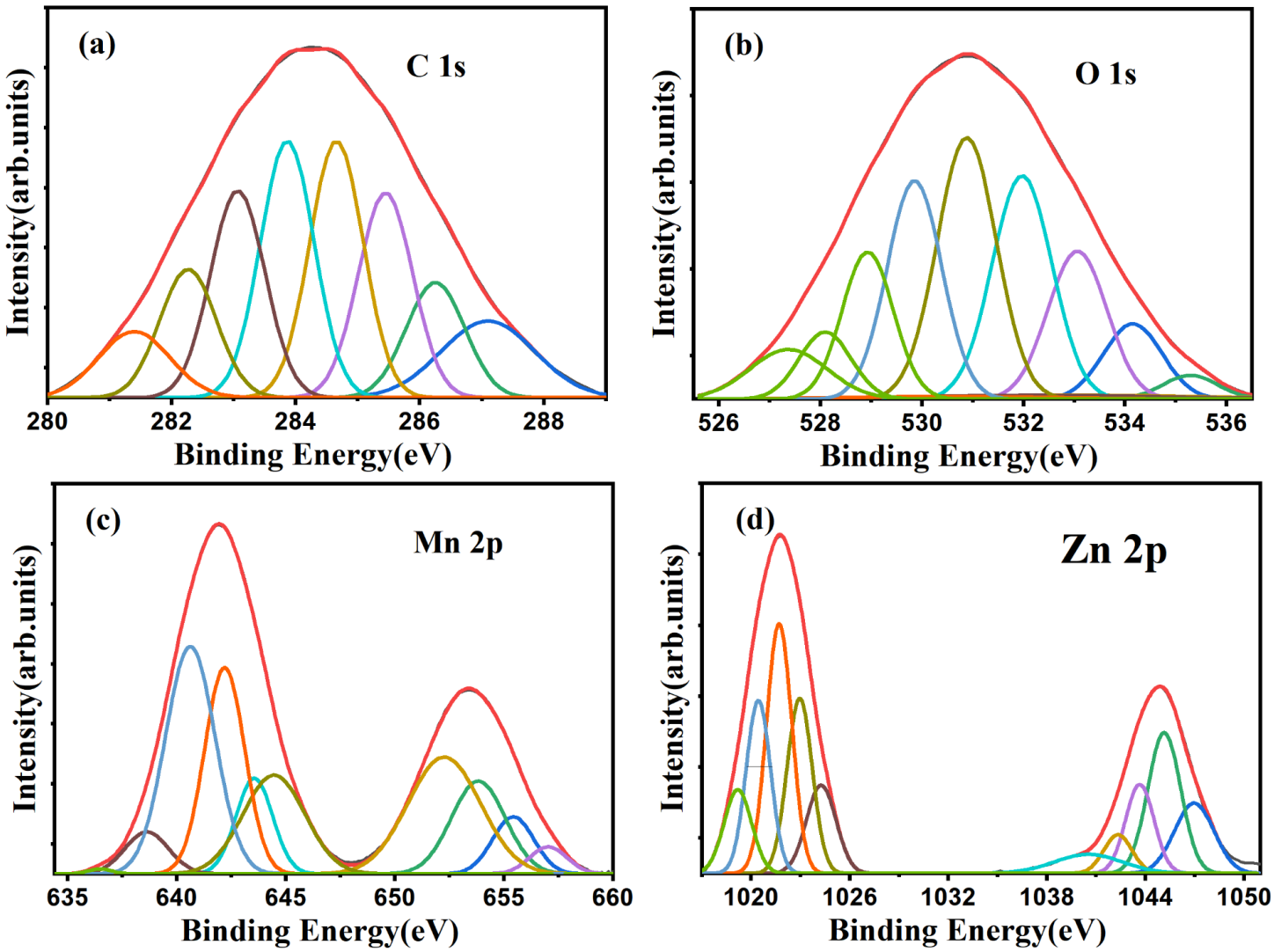


Figure 3

High-resolution XPS spectra of the Zn-MnO_2/G composite: (a) C 1s components ascribed to graphitic carbon and oxygen-containing carbon species; (b) O 1s components related to lattice, defect/hydroxyl, and adsorbed oxygen; (c) Mn 2p spin-orbit components consistent with mixed Mn^{3+} /Mn^{4+} states; and (d) Zn 2p components consistent with Zn^{2+}.

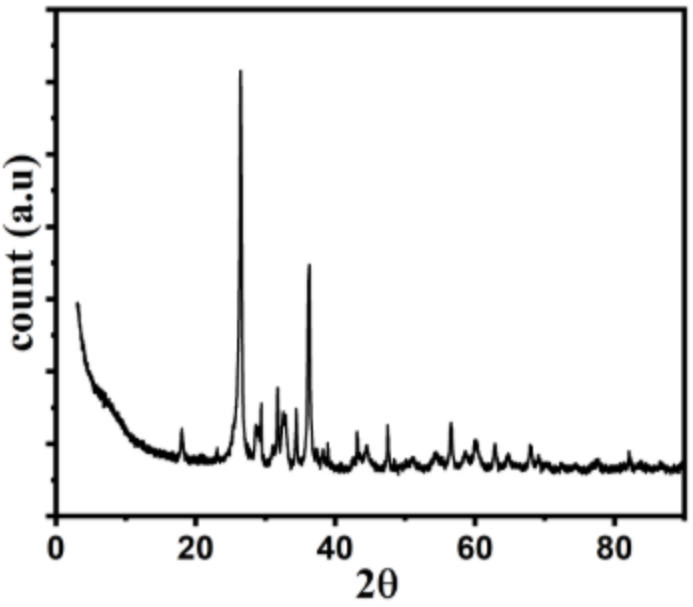


Figure 4

XRD pattern of the Zn-MnO_2/G composite. Crystallographic indexing should be completed from the original diffraction data using validated reference patterns before submission.

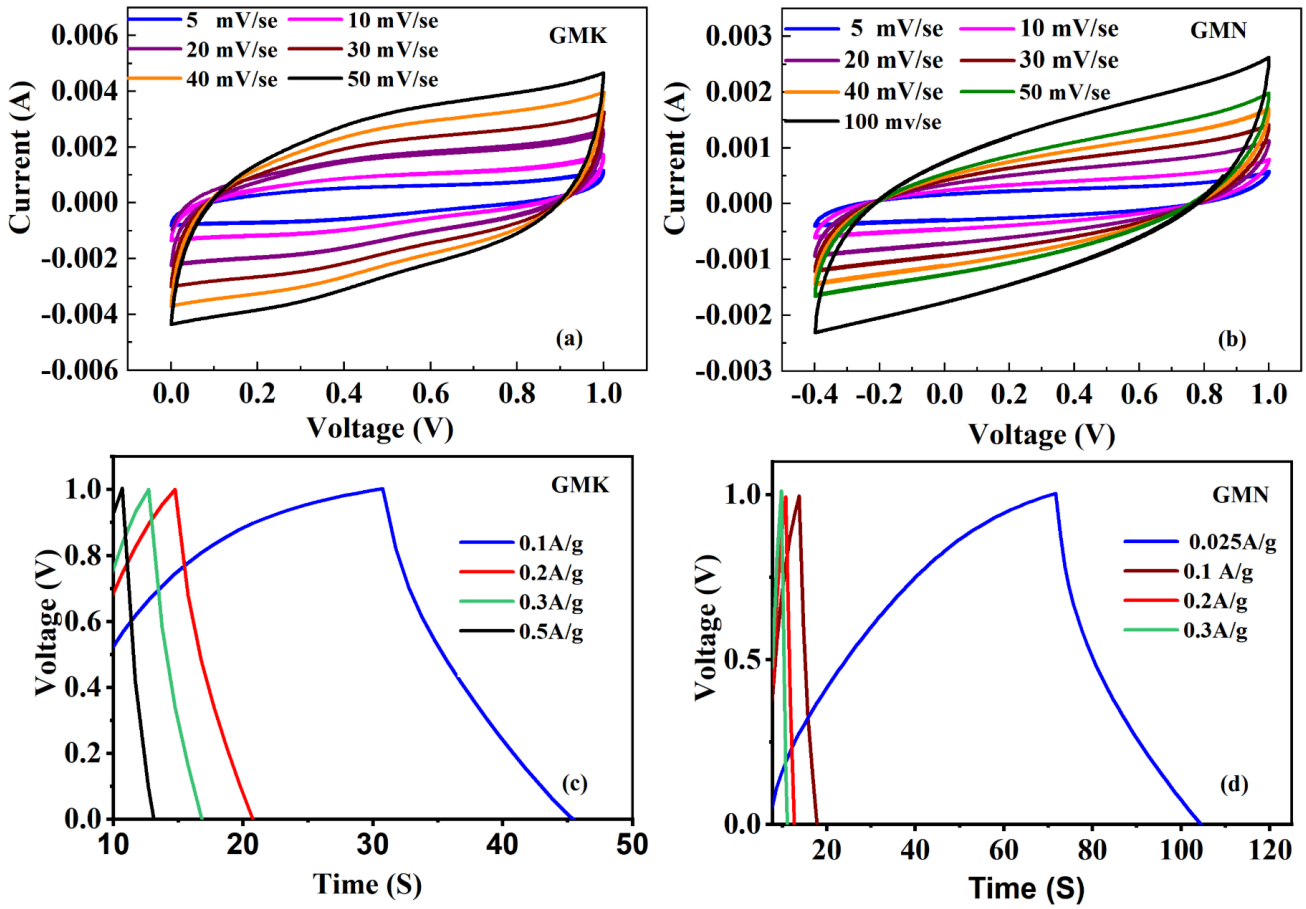


Figure 5

(a-b) Cyclic voltammetry curves of the symmetric Zn- MnO_2/G supercapacitor measured in aqueous electrolytes at different scan rates from 5 to 50 mV s-1. GMK and GMN denote KOH- and Na_2SO_4-based devices, respectively, wherever compared, (c-d) galvanostatic charge-discharge curves of the symmetric Zn- MnO_2/G supercapacitor in aqueous electrolyte at current densities from 0.1 to 0.5 A g^{-1}.

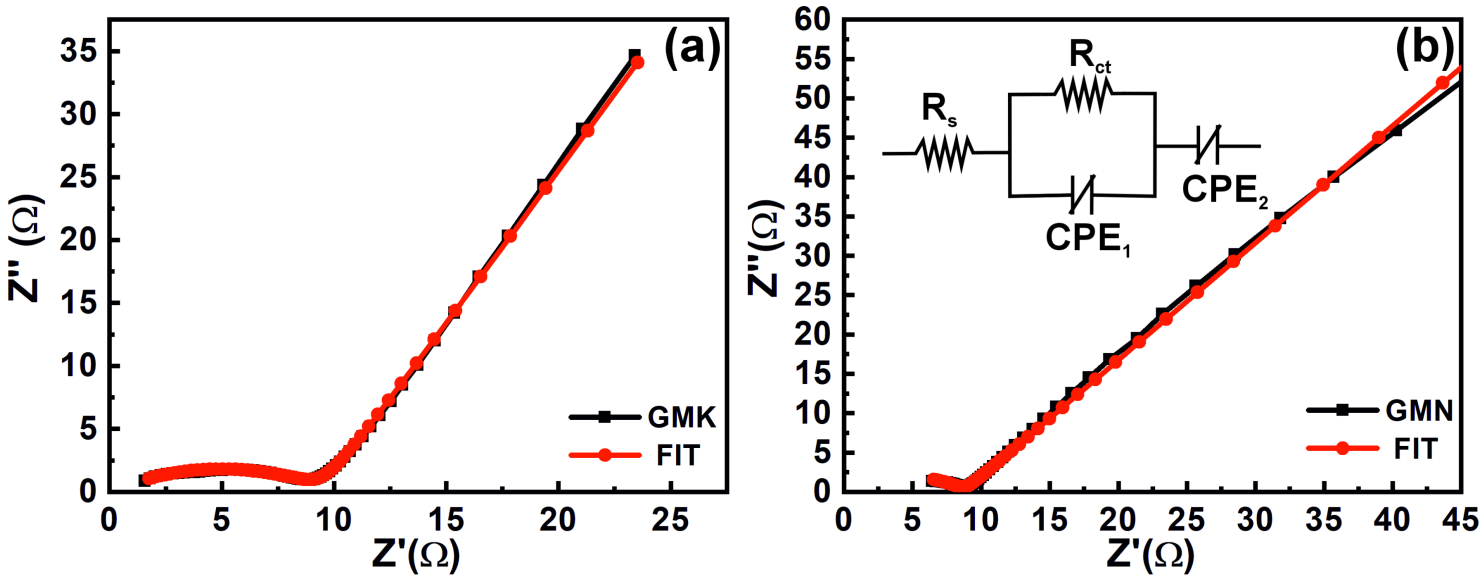


Figure 6

Nyquist plots of Zn–MnO_2–graphene electrodes measured in (a) KOH electrolyte, denoted as GMK, and (b) Na_2SO_4 electrolyte, denoted as GMN. The symbols represent the experimental EIS data, while the solid red lines represent the fitted curves obtained using the equivalent circuit R_s+(R_ct||CPE_1)+CPE_2. The lower impedance response and steeper low-frequency region of GMK indicate improved ion-transport behaviour and better capacitive performance in KOH electrolyte compared with Na_2SO_4.

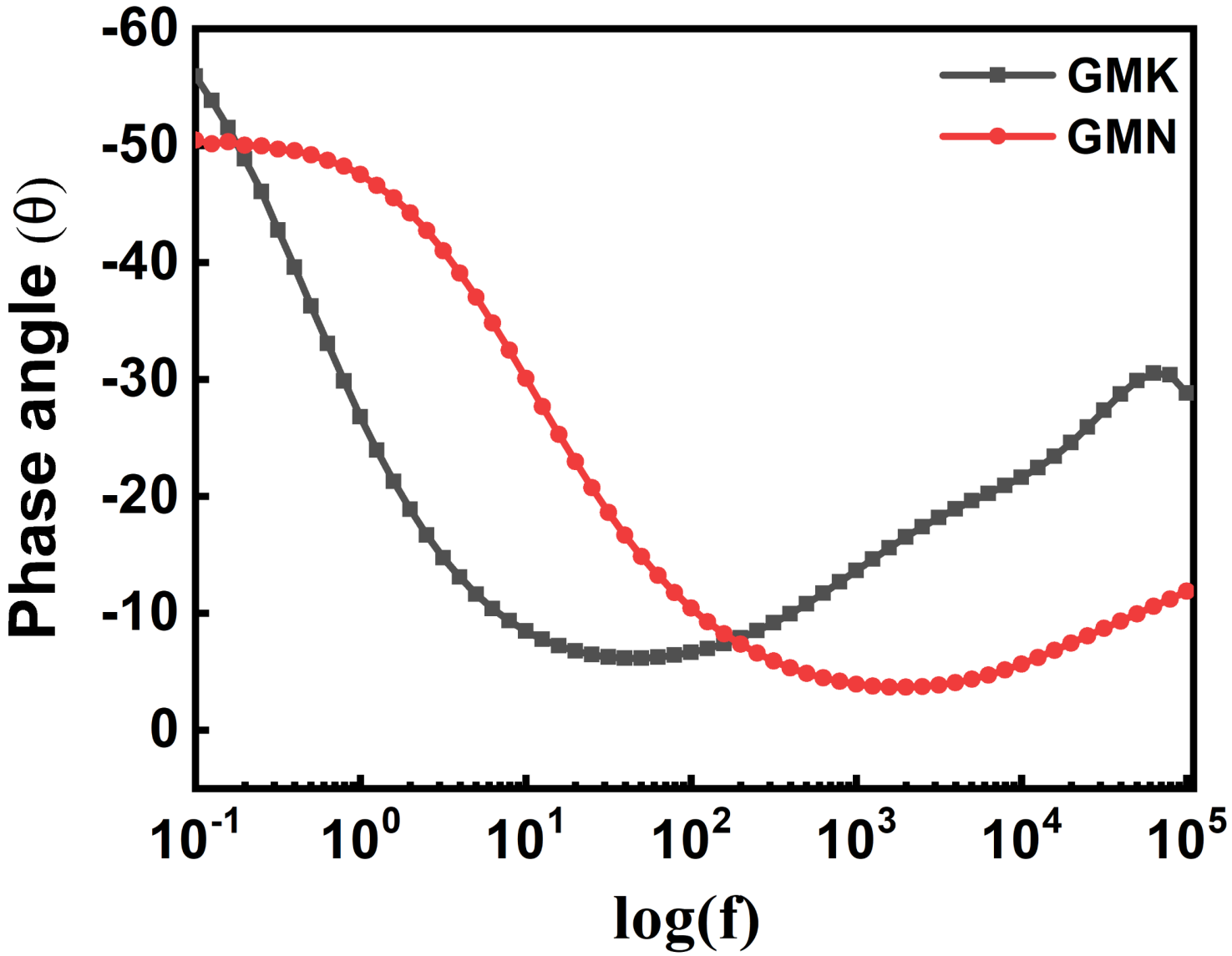


Figure 7

Bode-phase plots comparing GMK (KOH) and GMN (Na_2SO_4). The different phase-angle relaxation profiles demonstrate that electrolyte identity strongly affects capacitive response and ion/electron transport in the symmetric Zn-MnO_2/G devices.

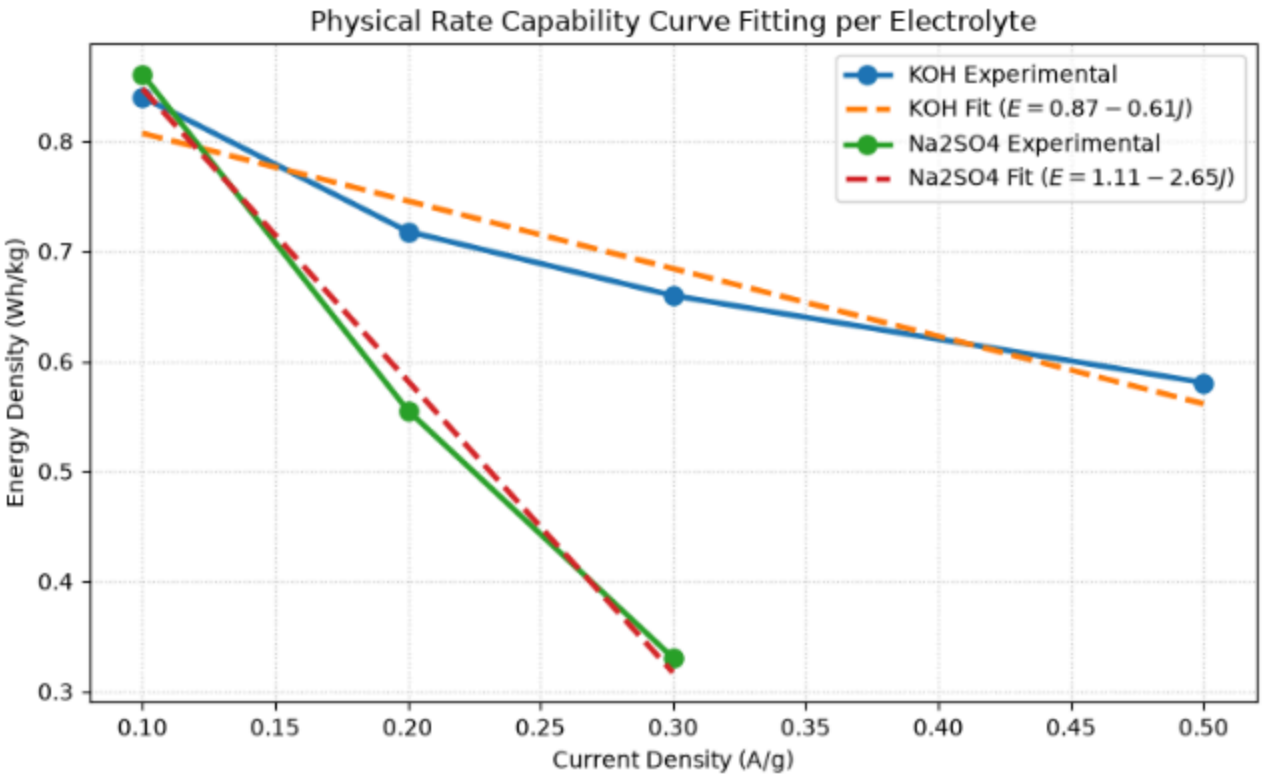


Figure 8

Experimental and fitted energy-density variation of Zn-doped MnO_2/G symmetric supercapacitors operated in KOH and Na_2SO_4 electrolytes as a function of current density. Symbols represent experimentally calculated energy-density values, while dashed lines represent fitting using the empirical physical rate-capability model . The lower rate-loss coefficient for the KOH electrolyte indicates better energy-density retention at higher current density compared with Na_2SO_4.